

# Comparing Jupiter’s equatorial X-ray emissions with solar X-ray flux over 19 years of the Chandra mission

Seán Christopher McEntee<sup>1,1</sup>, Caitriona M Jackman<sup>1,1</sup>, Dale M. Weigt<sup>2,2</sup>, William Dunn<sup>3,3</sup>, Vinay Kashyap<sup>4,4</sup>, Ralph P. Kraft<sup>4,4</sup>, Corentin Kenelm Louis<sup>2,2</sup>, Graziella Branduardi-Raymont<sup>3,3</sup>, Randy Gladstone<sup>5,5</sup>, and Peter Gallagher<sup>6,6</sup>

<sup>1</sup>Dublin Institute for Advanced Studies

<sup>2</sup>Dublin Institute for Advanced Studies (DIAS)

<sup>3</sup>University College London

<sup>4</sup>Smithsonian Astrophysical Observatory (SI)

<sup>5</sup>Southwest Research Institute

<sup>6</sup>DIAS

December 8, 2022

## Abstract

We present a statistical study of Jupiter’s disk X-ray emissions using 19 years of Chandra X-Ray Observatory (CXO) observations. Previous work has suggested that these emissions are consistent with solar X-rays elastically scattered from Jupiter’s upper atmosphere. We showcase a new Pulse Invariant (PI) filtering method that minimises instrumental effects which may produce unphysical trends in photon counts across the nearly-two-decade span of the observations. We compare the CXO results with solar X-ray flux data from the Geostationary Operational Environmental Satellites (GOES) X-ray Sensor (XRS) for the wavelength band 1-8 Å (long channel), to quantify the correlation between solar activity and jovian disk counts. We find a statistically significant Pearson’s Correlation Coefficient (PCC) of 0.9, which confirms that emitted jovian disk X-rays are predominantly governed by solar activity. We also utilise the high spatial resolution of the High Resolution Camera Instrument (HRC-I) on board the CXO to map the disk photons to their positions on Jupiter’s surface. Voronoi tessellation diagrams were constructed with the JRM09 (Juno Reference Model through Perijove 9) internal field model overlaid to identify any spatial preference of equatorial photons. After accounting for area and scattering across the curved surface of the planet, we find a preference of jovian disk emission at 2-3.5 Gauss surface magnetic field strength. This suggests that a portion of the disk X-rays may be linked to processes other than solar scattering: the spatial preference associated with magnetic field strength may imply increased precipitation from the radiation belts, as previously postulated.

# Comparing Jupiter's equatorial X-ray emissions with solar X-ray flux over 19 years of the Chandra mission

S.C. McEntee<sup>1,2</sup>, C.M. Jackman<sup>1</sup>, D.M. Weigt<sup>1</sup>, W. R. Dunn<sup>3,4</sup>, V. Kashyap<sup>5</sup>,  
R. Kraft<sup>5</sup>, C.K. Louis<sup>1</sup>, G. Branduardi-Raymont<sup>6</sup>, G. R. Gladstone<sup>7,8</sup>, P. T.  
Gallagher<sup>1,2</sup>

<sup>1</sup>School of Cosmic Physics, DIAS Dunsink Observatory, Dublin Institute for Advanced Studies, Dublin 15,  
Ireland

<sup>2</sup>School of Physics, Trinity College Dublin, Dublin, Ireland

<sup>3</sup>Department of Physics and Astronomy, University College London, London, UK

<sup>4</sup>Centre for Planetary Sciences at UCL/Birkbeck, London, UK

<sup>5</sup>Harvard-Smithsonian Center for Astrophysics, Smithsonian Astrophysical Observatory, Cambridge, MA,  
USA

<sup>6</sup>Mullard Space Science Laboratory, Department of Space and Climate Physics, University College  
London, Dorking, UK

<sup>7</sup>Space Science and Engineering Division, Southwest Research Institute, San Antonio, TX, USA

<sup>8</sup>Department of Physics and Astronomy, University of Texas at San Antonio, San Antonio, TX, USA

## Key Points:

- We present a statistical study of jovian disk X-rays from 19 years worth of Chandra data showing a strong correlation with solar X-ray flux.
- Jovian disk emissions are predominantly governed by solar activity. Pearson's Correlation Coefficient of 0.9 found between the data.
- Analysis of spatial morphology of the disk emissions reveals preference of disk emission at 2-3.5 Gauss magnetic field strength.

---

Corresponding author: Seán McEntee, [mcentees@tcd.ie](mailto:mcentees@tcd.ie)

This article has been accepted for publication and undergone full peer review but has not been through the copyediting, typesetting, pagination and proofreading process, which may lead to differences between this version and the [Version of Record](#). Please cite this article as [doi: 10.1029/2022JA030971](https://doi.org/10.1029/2022JA030971).

This article is protected by copyright. All rights reserved.

## Abstract

We present a statistical study of Jupiter's disk X-ray emissions using 19 years of Chandra X-Ray Observatory (CXO) observations. Previous work has suggested that these emissions are consistent with solar X-rays elastically scattered from Jupiter's upper atmosphere. We showcase a new Pulse Invariant (PI) filtering method that minimises instrumental effects which may produce unphysical trends in photon counts across the nearly-two-decade span of the observations. We compare the CXO results with solar X-ray flux data from the Geostationary Operational Environmental Satellites (GOES) X-ray Sensor (XRS) for the wavelength band 1-8 Å (long channel), to quantify the correlation between solar activity and jovian disk counts. We find a statistically significant Pearson's Correlation Coefficient (PCC) of 0.9, which confirms that emitted jovian disk X-rays are predominantly governed by solar activity. We also utilise the high spatial resolution of the High Resolution Camera Instrument (HRC-I) on board the CXO to map the disk photons to their positions on Jupiter's surface. Voronoi tessellation diagrams were constructed with the JRM09 (Juno Reference Model through Perijove 9) internal field model overlaid to identify any spatial preference of equatorial photons. After accounting for area and scattering across the curved surface of the planet, we find a preference of jovian disk emission at 2-3.5 Gauss surface magnetic field strength. This suggests that a portion of the disk X-rays may be linked to processes other than solar scattering; the spatial preference associated with magnetic field strength may imply increased precipitation from the radiation belts, as previously postulated.

## Plain Language Summary

The X-ray radiation that Jupiter emits from the region around the equator, or disk region, behaves differently to the auroral X-ray emissions (northern and southern lights). It has long been believed that these emissions are mainly caused by solar X-rays that reflect off of the planet's upper atmosphere, lighting up the disk. These high-energy X-ray emissions can be observed by the Earth-orbiting Chandra X-ray Observatory (CXO). There have been multiple X-ray campaigns of Jupiter using Chandra from 2000-2019. Here, we compare this data with solar X-ray data from the Geostationary Operational Environmental Satellites (GOES) satellite and identify a strong link between the disk X-ray emissions and solar activity. The High Resolution Camera on-board the CXO also enables us to pinpoint the location of these emissions, which we incorporate with magnetic field data from NASA's Juno to provide a more complete picture of the conditions at Jupiter's upper atmosphere.

## 1 Introduction

X-ray emissions from Jupiter have been observed since 1979, and were first detected by the imaging proportional counter and high resolution imaging detectors on the Einstein Observatory (Metzger et al., 1983), with the emissions characterised into the auroral (high-latitude) regions and the planetary disk (low- to mid-latitude). Differing driving mechanisms have been suggested to explain the properties of the X-rays emitted from these regions. Several studies have reported the strong conclusion that the X-rays emitted from Jupiter's planetary disk are likely to be correlated with solar X-rays, with spikes/peaks in the jovian light curve coincident with light travel-time-corrected Jupiter-facing solar flares (e.g. Bhardwaj et al., 2005, 2006; Elsner et al., 2005; Cravens et al., 2006; Branduardi-Raymont et al., 2007, 2010; W. R. Dunn et al., 2020a). This interpretation is based on data taken from the Chandra X-ray Observatory (Weisskopf et al., 2000) and the X-ray Multi-Mirror Mission (XMM-Newton) (Jansen et al., 2001), fitted with the EUV97 solar proxy model (Tobiska & Eparvier, 1998), that suggest the vast majority ( $\sim 90\%$ ) of disk X-ray emissions are produced from solar X-rays elastically scattered from Jupiter's upper atmosphere, with  $\sim 10\%$  fluorescent production of carbon K-shell X-rays from methane

74 (Maurellis et al., 2000; Cravens et al., 2006). Previous case studies have reported instances  
75 where the disk X-rays show similar day-to-day variability as the solar X-rays (Bhardwaj  
76 et al., 2005), with no evidence of the quasi-periodic flaring occasionally seen in the au-  
77 roral X-rays (e.g. Gladstone et al., 2002; Jackman et al., 2018; D. M. Weigt et al., 2021).

78 Branduardi-Raymont et al. (2010) found an apparent correlation between solar X-  
79 ray flux and disk X-ray power for both Jupiter and Saturn for a variety of observations.  
80 Furthermore, the equatorial spectrum of Jupiter during solar maximum is best fitted by  
81 coronal spectral models with temperatures in the energy range 0.4-0.5 keV, with addi-  
82 tional line emission from lines commonly seen in the solar X-ray spectrum at maximum  
83 activity and during flares, such as Mg XI (1.35 keV) and Si XIII (1.86 keV) (Branduardi-  
84 Raymont et al., 2007). W. R. Dunn et al. (2020a) states that the peak of the spectrum  
85 shifts to lower energies during the solar declining phase ( $0.29 \pm 0.02$  keV) and solar min-  
86 imum ( $0.18 \pm 0.02$  keV). This combination of spectral and temporal analysis, albeit from  
87 a small selection of case study events, has given further credence to the interpretation  
88 that the disk and auroral X-rays are produced by different processes. The auroral emis-  
89 sions can be split into hard X-rays ( $> 2$  keV), which result from X-ray bremsstrahlung,  
90 and soft X-rays ( $< 2$  keV), which are likely produced by charge exchange between pre-  
91 cipitating ions and neutrals in the jovian atmosphere (Elsner et al., 2005; Branduardi-  
92 Raymont et al., 2008; Houston et al., 2020). Alternatively, jovian disk X-ray emission  
93 is thought to be produced predominantly by scattering of solar X-rays in the jovian up-  
94 per atmosphere.

95 One other interesting property of the jovian disk emission is the observation of a  
96 small but statistically significant hour angle dependence in disk count rate and possi-  
97 ble link to surface magnetic field strength, with higher X-ray intensity in regions of low  
98 surface magnetic field strength (Waite et al., 1997; Gladstone et al., 1998; Elsner et al.,  
99 2005). This preferential emission of equatorial X-rays from regions of low surface mag-  
100 netic field can be explained by assuming these regions allow a larger atmospheric loss  
101 cone, which enables the precipitation of otherwise trapped ions and electrons from the  
102 radiation belts directly into the upper atmosphere, where they undergo charge-exchange  
103 interactions to produce X-rays (Waite et al., 1997). Indeed, Juno observations (Bolton  
104 et al., 2017) of the radiation belts show regions of low surface field strength where oth-  
105 erwise trapped populations are lost to the atmosphere (Kollmann et al., 2021). Exam-  
106 ination of the infrared (IR) emissions also showed a link to planetary magnetic field strength  
107 (Stallard et al., 2018), perhaps due to horizontal fields inhibiting the precipitation of  $H_2$   
108 into the atmosphere. Very recently, high resolution magnetic field data from the Juno  
109 spacecraft have revealed a region of intense localised magnetic field near Jupiter's equa-  
110 tor (Moore et al., 2018). Now that we have a highly resolved map of Jupiter's magnetic  
111 field thanks to Juno, as well as high spatial resolution X-ray measurements from CXO,  
112 we can make an analogous statistical map of the X-rays on the planet and quantitatively  
113 explore the links.

114 Since the earlier works on jovian disk X-rays, there have been a wealth of new ob-  
115 servations of Jupiter, scheduled to coincide with the in situ exploration by the NASA  
116 Juno spacecraft. The motivation for this study is to examine the complete catalogue of  
117 high spatial resolution Chandra observations (up to and including 2019) to quantify any  
118 correlation with solar X-ray flux, and to probe the distribution of photons across Jupiter.  
119 We will then investigate any significant clustering of emission in the context of local mag-  
120 netic anomalies or other dynamic processes at Jupiter. This is the first study of its kind  
121 to explore this over  $\sim$  two full solar cycles using the Chandra catalogue. The goals of  
122 this work include (i) tracking jovian X-rays from the planetary disk as a function of so-  
123 lar cycle, (ii) exploring the extent to which these disk X-rays correlate to solar X-ray ac-  
124 tivity, (iii) quantifying the spread of X-ray emission across the disk.

125 In this study, we utilise jovian X-ray data taken over 19 years with the Chandra  
126 X-ray Observatory's (CXO) High Resolution Camera (HRC), and compare them to cor-

127 responding solar X-ray flux data from the Geostationary Operational Environmental Satel-  
128 lites (GOES). Section 2 of this paper details the data set used in this study, and the pro-  
129 cessing methods that were employed to ensure consistency across the time span of the  
130 data. Section 3 shows results from temporal and spatial analyses of the data set, and  
131 Section 4 offers an interpretation of the results and poses questions for future investi-  
132 gation.

## 133 2 Data Sets and Methods

### 134 2.1 Data Sets

135 The Chandra X-ray Observatory (CXO) conducted observations of Jupiter 29 times  
136 between 2000 and 2019 using the on-board High-Resolution Camera Imaging (HRC-I)  
137 instrument. The HRC-I contains a single large-format microchannel plate, providing high  
138 spatial resolution of  $\sim 0.4$  arcsec over a  $30 \text{ arcmin} \times 30 \text{ arcmin}$  field of view. The best  
139 image quality is found in the centre of the field of view, where the camera's aim point  
140 is located. This allows for the X-ray time-tagged photons to be mapped to their specific  
141 location on Jupiter's surface in System III (SIII) latitude and SIII longitude (where Sys-  
142 tem III is a left-handed co-ordinate system which rotates with the planet, and where the  
143 z-axis is defined by the spin axis of Jupiter). HRC-I is however limited by its poor en-  
144 ergy resolution, rendering it unable to distinguish between hard and soft X-rays. Of this  
145 data set, 21 observations have taken place since 2016 (starting with Juno's approach and  
146 arrival at Jupiter). Many of the Juno-era observations were taken near the perijoves of  
147 the Juno spacecraft, with a few timed to coincide with apojove, or with other key mag-  
148 netospheric encounters (such as current sheet crossings). The remaining observations co-  
149 cided with campaigns in other wavelenghts (including Hubble Space Telescope (HST)  
150 UV auroral observations). Table 1 shows key descriptors of each of the Chandra HRC-  
151 I observations. The Earth-Jupiter (E-J) distances, Sun-Jupiter (S-J) distances, Sun-Earth  
152 (S-E) distances and Earth-Sun-Jupiter (E-S-J) angles were all obtained using the JPL  
153 Horizons program (data available at <https://ssd.jpl.nasa.gov/horizons/app.html#/>).

154 We use the same 29 observations which were explored in a statistical study by D. M. Weigt  
155 et al. (2021) of the northern auroral emissions. Like that study, one observation is omit-  
156 ted (ObsID 18303) due to Jupiter's position on the chip of the detector being shifted away  
157 from the aim point. The result of this misalignment was that the mapping procedure could  
158 not be performed accurately as the point spread function (PSF) increases with distance  
159 from the centre of the detector, leading to large uncertainties. The 28 HRC-I observa-  
160 tion times are displayed in panel (a) of Figure 1 (blue vertical lines) overplotted to the  
161 smoothed monthly sunspot number to give an indication of the coverage of jovian X-ray  
162 observations with solar cycle. The calculation of the count rates which appear in pan-  
163 els (b) and (c) will be discussed in detail later in Section 2.2.3.

164 In addition to Chandra data, we utilise data from the Geostationary Operational  
165 Environmental Satellites (GOES), a constellation of satellites which orbit the Earth in  
166 a geosynchronous orbit, with near-constant viewing of the Sun. The X-ray Sensor (XRS)  
167 on-board has the ability to monitor changes in solar X-ray flux with 3-second time res-  
168 olution over the corresponding time window of HRC-I observations of Jupiter. GOES  
169 XRS provides solar X-ray fluxes for the wavelength band  $1\text{-}8 \text{ \AA}$  (long channel), corre-  
170 sponding to an energy range  $1.55\text{-}12.4 \text{ keV}$ . In comparison, Jupiter's disk emissions dur-  
171 ing solar maximum are dominated by Fe-lines that peak at  $0.7\text{-}0.9 \text{ keV}$ , with further con-  
172 tributions from Ne and Mg up to  $1.5 \text{ keV}$ . However, the peak of this spectrum shifts to  
173 lower energies during the solar declining phase and solar minimum (W. R. Dunn et al.,  
174 2020a). This discrepancy between the energy ranges of the respective satellites means  
175 that the lower limit of the XRS energy range will exceed the peak of the jovian disk X-  
176 ray brightness. Unfortunately, there are no solar X-ray data available in the  $0.1\text{-}1.5 \text{ keV}$   
177 range to compare with the jovian disk X-rays.

ObsID	Start Date (year-month-day hr:min:s)	Exp Time (ks)	Disk Counts	Net Disk Count Rate (cts/ks/px <sup>2</sup> )	E-J Distance (AU)	S-J Distance (AU)	S-E Distance (AU)	E-S-J Angle (deg)
*1862	2000-12-18 09:54:27	37	1840	$4.69 \times 10^{-4}$	4.13	5.04	0.98	19.05
†2519	2003-02-25 00:22:24	72	1498	$1.35 \times 10^{-4}$	4.41	5.32	0.99	21.48
*15669	2014-04-15 20:44:11	40	926	$2.32 \times 10^{-4}$	5.37	5.23	1.00	92.29
*15670	2014-04-20 02:20:37	42	756	$0.81 \times 10^{-4}$	5.43	5.23	1.01	96.08
†15671	2014-04-08 08:19:16	43	1001	$2.21 \times 10^{-4}$	5.25	5.23	1.00	85.55
†15672	2014-04-12 22:10:37	42	876	$1.89 \times 10^{-4}$	5.32	5.23	1.00	89.66
*16299	2014-04-10 01:10:29	40	991	$2.61 \times 10^{-4}$	5.27	5.23	1.00	87.06
*16300	2014-04-17 12:20:38	42	937	$2.17 \times 10^{-4}$	5.39	5.23	1.00	93.78
†18301	2017-02-02 09:58:06	35	937	$-0.01 \times 10^{-4}$	5.03	5.46	0.99	59.45
†18302	2017-05-19 00:28:41	43	1404	$0.18 \times 10^{-4}$	4.69	5.46	1.01	37.12
*18608	2016-05-24 10:23:06	42	967	$0.25 \times 10^{-4}$	5.18	5.44	1.01	69.74
†18609	2016-06-01 11:32:08	42	914	$0.14 \times 10^{-4}$	5.30	5.44	1.01	76.85
18676	2017-03-27 08:32:05	11	326	$0.02 \times 10^{-4}$	4.48	5.46	1.00	10.53
†18677	2017-07-10 21:12:27	42	1081	$0.25 \times 10^{-4}$	5.43	5.45	1.02	83.66
†18678	2018-03-31 23:11:51	41	1311	$0.15 \times 10^{-4}$	4.62	5.42	1.00	34.05
†18679	2018-05-24 00:00:53	42	1457	$0.15 \times 10^{-4}$	4.43	5.41	1.01	13.55
†18680	2018-09-06 20:39:56	43	895	$0.17 \times 10^{-4}$	5.75	5.38	1.01	106.74
†20000	2017-02-28 12:40:03	74	2422	$0.09 \times 10^{-4}$	4.68	5.46	1.00	34.86
†20001	2017-06-18 18:39:05	39	1063	$0.12 \times 10^{-4}$	5.09	5.45	1.02	64.23
†20002	2017-08-06 01:56:57	38	757	$-0.05 \times 10^{-4}$	5.82	5.45	1.01	106.67
†20733	2018-04-01 10:39:09	41	1264	$-0.04 \times 10^{-4}$	4.62	5.42	1.00	33.62
22146	2019-07-13 01:27:31	27	865	$0.12 \times 10^{-4}$	4.42	5.29	1.02	28.47
22147	2019-07-13 21:09:39	25	798	$0.13 \times 10^{-4}$	4.43	5.29	1.02	29.18
22148	2019-07-15 13:00:05	27	827	$-0.01 \times 10^{-4}$	4.44	5.29	1.02	30.64
22149	2019-07-16 08:45:59	27	941	$0.53 \times 10^{-4}$	4.45	5.29	1.02	31.36
22150	2019-07-18 20:19:01	27	904	$0.40 \times 10^{-4}$	4.48	5.29	1.02	33.52
22151	2019-09-08 22:59:25	27	705	$0.39 \times 10^{-4}$	5.18	5.27	1.01	79.40
†22159	2019-05-29 03:27:35	38	1305	$0.07 \times 10^{-4}$	4.31	5.30	1.01	10.79

**Table 1.** List of Chandra HRC-I observations of Jupiter from 2000-2019, including the Observation ID (ObsID), exposure time, disk counts, net disk count rate, Earth-Jupiter (E-J) distance, Sun-Jupiter (S-J) distance, Sun-Earth (S-E) distance and Earth-Sun-Jupiter (E-S-J) angle. One observation (ObsID 18303) is omitted from the data set due to Jupiter’s position on the chip of the detector being shifted away from the aim point.

\*Relative high solar activity cases (as defined in section 3.1).

†Relative low solar activity cases.

For this study, data were consistently available from the G10 satellite for CXO observations prior to 2011, and the G15 satellite supplied data for all observations over the period 2014-2019. The data from these satellites, and the comparison with the corresponding jovian disk light-curves, are analysed in Section 3.1.

In order to be able to quantitatively compare the number of jovian disk counts obtained for observations spanning this 19-year interval, it is critical that the processing pipeline takes account of any instrumental changes over time. For this, we needed to develop a new filtering method for the jovian X-ray photons and the off-Jupiter X-ray background, discussed below in Section 2.2.

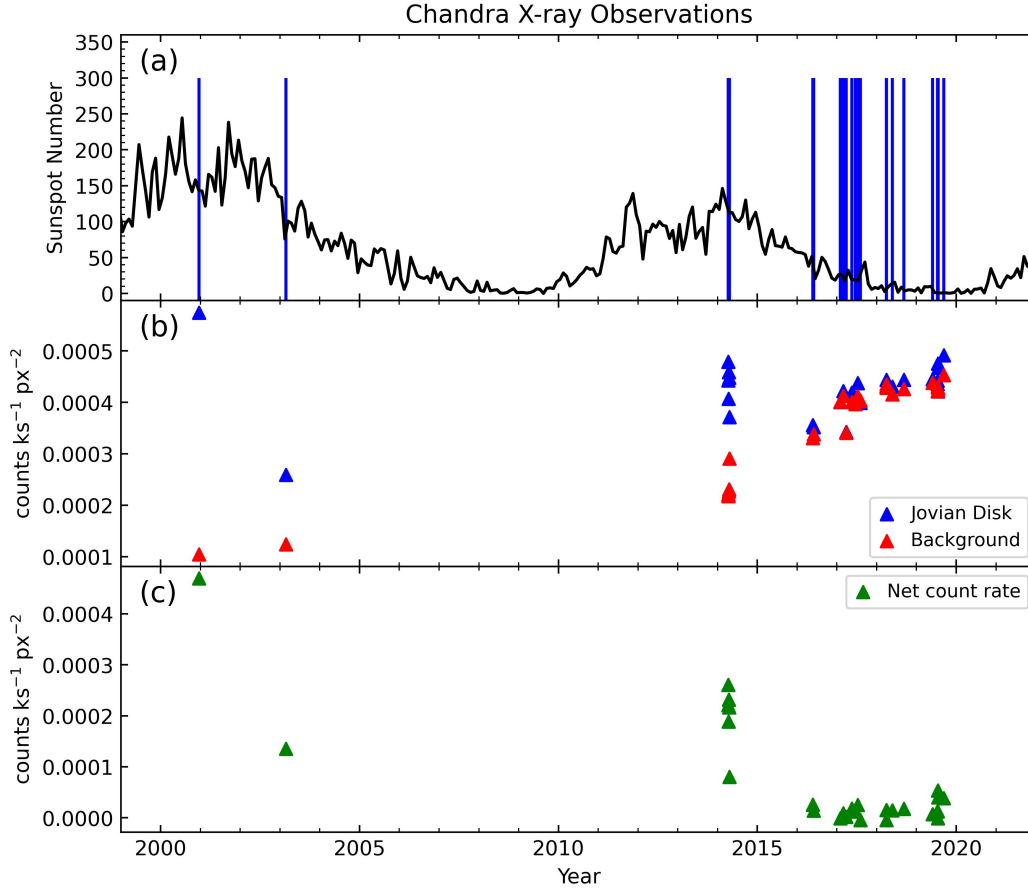


**Figure 1.** Chandra X-ray observations of Jupiter from 2000-2019. (a) Monthly sunspot number (from SIDC <https://www.sidc.be/silso/home>) with times of CXO observations overlaid by vertical lines. (b) Jovian disk (blue) and background (red) count rates per unit area (cts ks<sup>-1</sup> px<sup>-2</sup>) for each HRC-I observation of Jupiter. (c) Net count rate (green) of jovian disk after subtracting the background (cts ks<sup>-1</sup> px<sup>-2</sup>). Disk region defined as latitudes from -55° to +45° SIII lat.

187

## 2.2 Methods

188

### 2.2.1 Updates to Mapping Algorithm and Photon Selection Pipeline

189

190

191

192

193

194

195

196

197

198

The raw data obtained from HRC-I first have to be transformed into a frame of reference centred on Jupiter. This is done using the SSO\_FREEZE algorithm (see [https://cxc.cfa.harvard.edu/ciao/ahelp/sso\\_freeze.html](https://cxc.cfa.harvard.edu/ciao/ahelp/sso_freeze.html)), which uses appropriate ephemerides data from the JPL Horizons program and Chandra orbit ancillary data from the Chandra X-ray Center to account for Jupiter’s motion on the sky and the relative position of the detector. The raw data are reprojected from sky x and y co-ordinates to a reference frame which is fixed to the motion of Jupiter. This helps to eliminate the “blurring” seen in the sky x and y co-ordinates. Figure 2 shows the output images in both (a) sky co-ordinates and (b) Jupiter centred co-ordinates. The streaks in (a) display the motion of Jupiter’s northern and southern aurorae across the detector.

199

200

201

202

Once completed, a separate GO\_CHANDRA algorithm (Gladstone et al., 2002) is employed to map the time-tagged photons to their respective positions on Jupiter’s surface, which enables the selection of photons according to their positions and times. In previous versions of this algorithm used in published works (Gladstone et al., 2002; Jack-

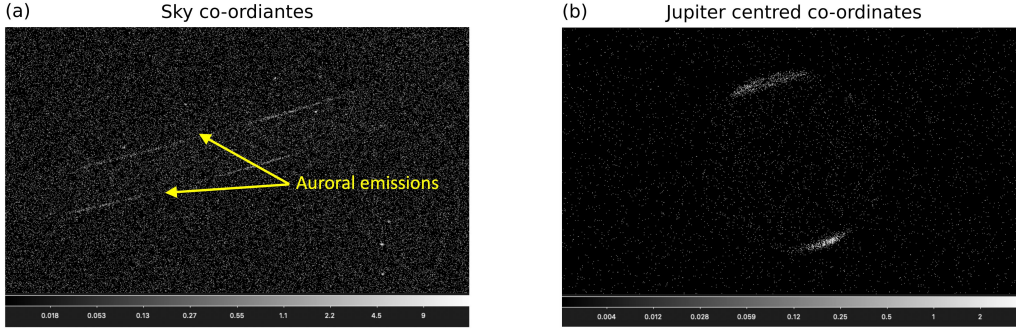


**Figure 2.** Chandra HRC-I output files in (a) sky co-ordinates and (b) Jupiter centred co-ordinates. Transformation between (a) and (b) was done using the SSO.FREEZE algorithm. Colourbars are in units of counts.

man et al., 2018; D. M. Weigt et al., 2020), Jupiter was centred on the centre of the chip on HRC-I, and a circle of radius 30 arcsec was drawn around the planet, including all photons within this region. This approximation used by the algorithm is sufficient when looking at the more intense auroral emissions at the poles (e.g. Gladstone et al., 1998; Elsner et al., 2005). When analyzing the disk emissions however, we want to ensure that we reduce the contamination from X-rays outside of Jupiter’s disk. As a result, we have produced a new update to this photon selection procedure, which incorporates the ellipticity of Jupiter, and generates a tilted ellipse based on the tilt angle of Jupiter’s north pole and the planet’s angular diameter (both quantities obtained via JPL Horizons). Photons are selected on the basis of whether they lie within this ellipse region. The result is that this updated method better constrains the limb of Jupiter, thus removing a significant proportion of sky background counts located near the limb of the planet that were previously included as jovian photons (see Figure 3). All data analysis procedures discussed in this study are provided at <https://doi.org/10.5281/zenodo.5657142> (McEntee, 2021).

### 2.2.2 Pulse Invariant (PI) Filtering Method

Maintaining consistency is crucial when compiling a data set over such a large time span, particularly when using quantitative information such as total photon counts to infer information about the level of jovian activity and solar driving. Over time, instrument degradation becomes a key factor on-board CXO. In the case of HRC-I, the gain of the instrument has been decreasing over time (see [https://cxc.cfa.harvard.edu/cal/Hrc/Documents/Gain/hrci\\_sampgain\\_nov2009.pdf](https://cxc.cfa.harvard.edu/cal/Hrc/Documents/Gain/hrci_sampgain_nov2009.pdf)), and the calibration team at Chandra have developed procedures to measure this trend (Posson-Brown & Kashyap, 2007). Originally, the nominal gain metric for HRC was the Pulse Height Amplitude (PHA), which gave the sum of all detector amplifier signals. Another quantity, the scaled sum of amplifier signals (SUMAMPS), gives the sum of signals from the three amplifiers nearest the X-ray photon signal on each axis. For HRC-I, the PHA values are limited by saturation at PHA=255, while SUMAMPS are not, thus providing a better capability for spectral discrimination. Due to the superiority of SUMAMPS for gain measurements on HRC, scaled SUMAMPS (SAMP) has become the standard gain measure. The spatial variance of SAMP is much less than for PHA, and it also has the advantage of not being integerised. The scaling is done by the amplifier scale factor values ( $AMP\_SF$ ) as follows:

$$SAMP = \frac{SUMAMPS \times 2^{AMP\_SF-1}}{C}, \quad (1)$$

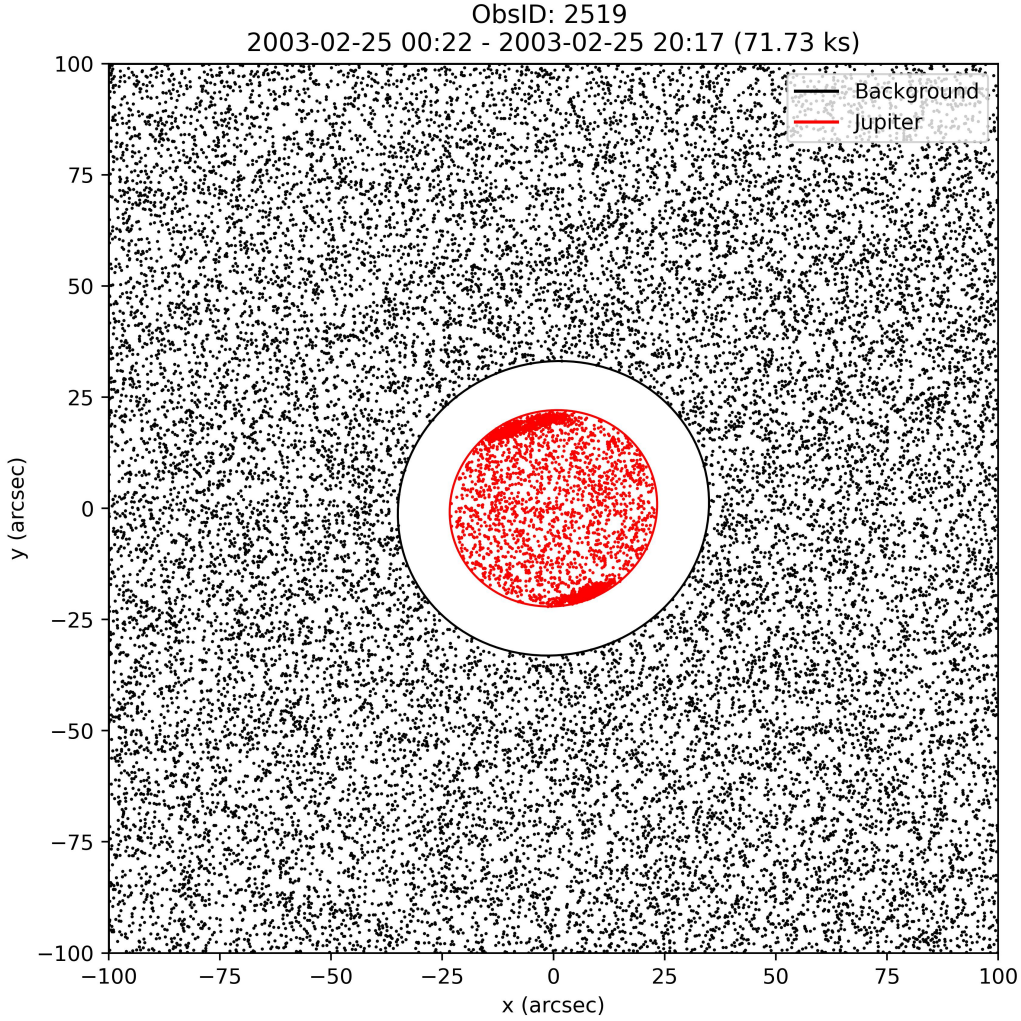


**Figure 3.** Example of the typical output of the GO\_CHANDRA photon selection algorithm, showing the ellipse region (red) constrained to the limb of the planet. Background photons are shown in black. Photons that lie neither on Jupiter nor within the background region have not been included, so the space between these regions is completely empty.

where  $C$  is a constant. For HRC-I,  $C=148$ , and this value is chosen so that the SAMP and PHA distributions match closely. The SAMP and PHA distributions shift to lower channels over time as the gain of HRC-I decreases. To account for this, another quantity, called Pulse Invariant (PI), is introduced. This quantity removes the time-dependence of the SAMP values, creating a distribution similar to that produced at the beginning of the Chandra mission. SAMP can be converted to PI using a multiplicative gain correction factor,  $g$ :

$$PI = g \times SAMP, \quad (2)$$

where

$$g = 1.0418475 + 0.020125799 (Y - 2000) + 0.010877227 (Y - 2000)^2 - 0.0014310146 (Y - 2000)^3 + (5.8426766 \times 10^{-5}) (Y - 2000)^4,$$

219 where  $Y$  is the start of the observation in decimal year.

220 After the PI has been calculated for each X-ray photon detected, we then apply  
 221 a filter to the source (Jupiter) PI spectrum whereby we only include photons if they lie  
 222 in the PI channel range 10-250. This channel range was selected to contain the region  
 223 of the PI spectrum where the source dominates the background. The corresponding PI  
 224 range is then applied to our X-ray background spectrum, removing a larger (in general)  
 225 percentage of background than that removed from the source. Our background region  
 226 is defined as the area outside an ellipse 1.5 times the size of Jupiter, and inside a square  
 227 region of length 200 arcsec, shown in Figure 3 as the black region. Photons that do not  
 228 emanate from Jupiter and are not contained within the background region are not in-  
 229 cluded in Figure 3, resulting in the white space that is observed between the boundaries  
 230 of the planet (red) and background (black) regions.

231 This important additional step ensures that we remove as much background con-  
 232 tamination from our Jupiter region and should be applied to archival and upcoming Chan-  
 233 dra data. We note that these effects occur with observations of other planets such as Sat-  
 234 urn (D. Weigt et al., 2021) and Uranus (W. Dunn et al., 2021) and should be applied  
 235 to all CXO HRC-I planetary observations.

### 236 *2.2.3 Disk Region Selection*

237 In order to obtain the disk count rates for each of the 28 HRC-I observations of Jupiter  
 238 that are displayed in panel (b) of Figure 1, we first must define the boundaries of the  
 239 jovian disk. This constraint on latitude was defined using the total X-ray map illustrated  
 240 in Figure 4. This figure contains the summed total of all jovian photons across the en-  
 241 tire data set, binned into  $5^\circ$  SIII longitude  $\times$   $5^\circ$  SIII latitude bins. The colourbar  
 242 was also saturated at 40 counts/bin to visualise structure on the disk. The boundaries were  
 243 imposed at latitudes where there was a clear end to the northern and southern aurorae.  
 244 These boundaries were found to be  $+45^\circ$  SIII latitude in the north and  $-55^\circ$  SIII lati-  
 245 tude in the south. We utilise the method presented in Bhardwaj et al. (2006) by fitting  
 246 a rectangular box over color-coded two-dimensional histograms of Chandra data to iso-  
 247 late the planetary disk region (see Figure 1). Our boundaries take into account the sta-  
 248 tistical picture over 19 years and reflect a desire to be conservative so as to not erroneously  
 249 include auroral photons, but also to encompass as much of the disk as possible. There-  
 250 fore, Figure 4 can be split into three different regions:

- 251 • Northern Auroral Region ( $> +45^\circ$  SIII latitude),
- 252 • Southern Auroral Region ( $< -55^\circ$  SIII latitude),
- 253 • Planetary Disk Region ( $-55^\circ$  to  $+45^\circ$  SIII latitude).

254 This latitude constraint was used to determine the jovian disk count rates for the  
 255 HRC-I observations that are included in Figure 1(b). The jovian disk count rate, along  
 256 with that of the background region (as defined in Figure 3), were then divided by the  
 257 areas of the respective regions (in units of  $\text{px}^2$ ) to give the final count rates that appear  
 258 in Figure 1(b). Finally, the background was subtracted from the jovian disk count rate  
 259 to yield the net disk count rates seen in Figure 1(c). These net disk count rates are also  
 260 displayed in Table 1.

### 261 *2.2.4 Voronoi Tessellation Algorithm*

262 As discussed earlier, the high spatial resolution of HRC enables the mapping of time-  
 263 tagged jovian photons that strike the detector back to their specific location on Jupiter's  
 264 surface in SIII longitude and SIII latitude. The spatial morphology of these photons can  
 265 then be investigated in further detail. For this purpose, we employ Voronoi tessellation  
 266 diagrams, based on the VOISE (VORonoi Image SEGmentation) algorithm (Guio & Achilleos,  
 267 2009). In this method, each photon, or “seed”, has a given location in SIII longitude and  
 268 SIII latitude. A polygon is then drawn around each seed, enclosing the area that is closer

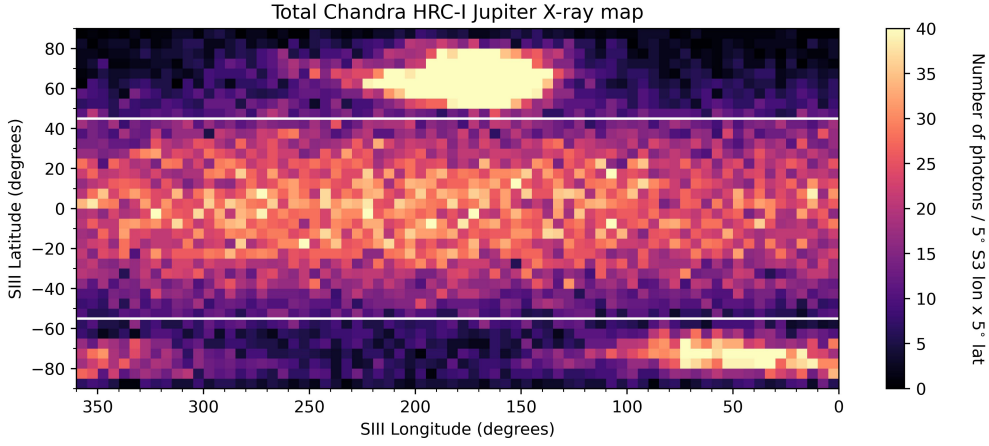


**Figure 4.** X-ray heatmap containing the photons detected from all 28 HRC-I observations of Jupiter from 2000-2019. Photons are binned into  $5^\circ$  SIII longitude  $\times$   $5^\circ$  SIII latitude bins and the colourbar is saturated at 40 photons per bin to display structure on the disk. White horizontal lines represent the latitude boundaries of the disk region, which are  $45^\circ$  SIII latitude in the north and  $-55^\circ$  SIII latitude in the south.

269 to that seed than any other. Therefore, there are the same number of polygons in the  
 270 grid as seeds/photons. The result is a spatial map where the concentration of photons  
 271 can be quantified and compared between different observations by calculating the areas  
 272 of the polygons ( $\text{deg}^2$ ). Observations which contain a large number of photons will pro-  
 273 duce a Voronoi tessellation diagram containing many low-area polygons. Conversely, a  
 274 more sparse data set will result in a spatial map containing large polygons of high area.  
 275 This method was chosen for the spatial analysis in this study as it provides a more au-  
 276 tomatized and objective method of investigating the spatial morphology of the jovian disk  
 277 X-ray photons.

### 278 3 Results and Discussion

279 We wish to examine the temporal and spatial properties of Jupiter's disk emissions  
 280 in order to move towards a quantitative understanding of their generation mechanism.

#### 281 3.1 Sun-Jupiter X-ray connection

282 Figure 5 shows comparisons of the net jovian disk (CXO) and the solar X-ray (GOES  
 283 XRS) light curves. Two examples are shown, coinciding with relatively high (a, b) and  
 284 low (c, d) solar activity. The levels of solar activity were determined on the basis of whether  
 285 the peak GOES X-ray flux over the observation window exceeded a quantitative thresh-  
 286 old of  $10^{-6} \text{ Wm}^{-2}$ . This threshold was chosen as it represents the mean of our data set,  
 287 with the peak flux ranging from  $2.3 \times 10^{-8}$  to  $7.2 \times 10^{-6} \text{ Wm}^{-2}$ . The cases used in  
 288 this comparison were chosen because they represent the extremes of our data set in terms  
 289 of Jupiter-Earth (J-E) distance (4.13 vs 5.82 AU). Furthermore, both observations have  
 290 an exposure time approximately equal to one full jovian rotation. Panels (a) and (c) of  
 291 Figure 5 show the net count rates per unit area of Jupiter's disk region ( $\text{cts min}^{-1} \text{ px}^{-2}$ )  
 292 after subtracting the associated particle background for each observation, with the data  
 293 binned into 5-minute bins. The CXO data are shifted backwards in time by the time dif-  
 294 ference between Sun-Jupiter-Earth and Sun-Earth light travel times. In this way, we are  
 295 directly comparing the solar flux observed by GOES to the jovian disk photons that are

296 detected by HRC-I on board the CXO. The raw GOES data are included with 3-second  
 297 time resolution.

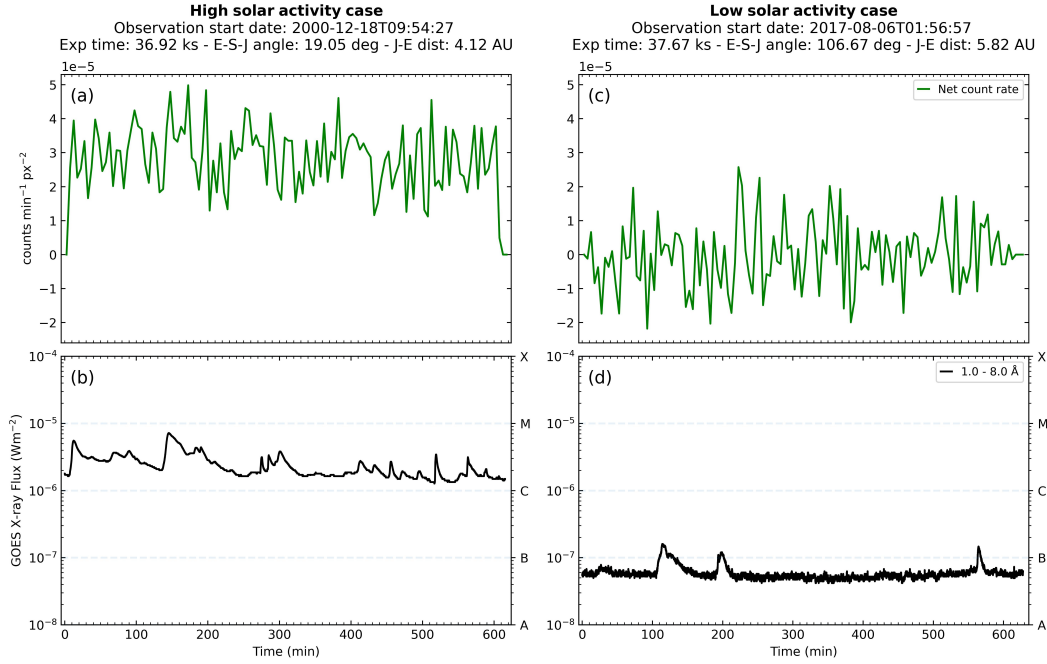


**Figure 5.** Comparison between HRC-I jovian disk net light-curve (energy range 0.06-10 keV) and GOES solar X-ray flux (long channel, wavelength band 1-8 Å) for observations that coincided with (a, b) relatively high (ObsID 1862, 18 December 2000) and (c, d) low solar activity (ObsID 20002, 6 August 2017). Jovian disk light-curves are shown in 5-minute bins. The CXO data are shifted backwards in time by the time difference between Sun-Jupiter-Earth and Sun-Earth light travel times. The raw GOES data are used with 3-second time resolution.

298 The GOES solar X-ray flux light curves show a greater than order of magnitude  
 299 change in the baseline flux between the high solar activity case (Figure 5(b)) and the low  
 300 solar activity case (Figure 5(d)). This change is accompanied by a similar change in the  
 301 jovian disk net light curve per unit area, indicating that this increase in the net count  
 302 rate is influenced by the increase in solar X-ray flux. In order to quantify this link, we  
 303 must extrapolate this finding to include our entire data set.

304 Figure 6 shows the net count rate (cts min<sup>-1</sup> px<sup>-2</sup>) of the jovian disk region for  
 305 each of the 28 HRC-I observations of Jupiter, plotted against the median GOES solar  
 306 X-ray flux (Wm<sup>-2</sup>) over the corresponding observation window. The data sets are found  
 307 to be in good agreement, with a Pearson's Correlation Coefficient (PCC) of 0.9. This  
 308 provides clear evidence that the vast majority of the X-ray emissions emanating from  
 309 Jupiter's planetary disk region are indeed consistent with solar X-rays elastically scatter-  
 310 ed from the planet's upper atmosphere.

### 311 3.2 Spatial morphology of jovian disk

312 In addition to looking at the correlation between the jovian disk X-rays and solar  
 313 X-ray flux, the high spatial resolution of HRC allowed for the investigation of the spa-  
 314 tial morphology of the disk photons. This analysis was conducted to explore the possi-  
 315 bility of any spatial preference of X-ray emission across the disk region. For this sur-

Net Disk Count Rate vs Median Solar X-ray Flux  
 Pearson's Correlation: 0.9

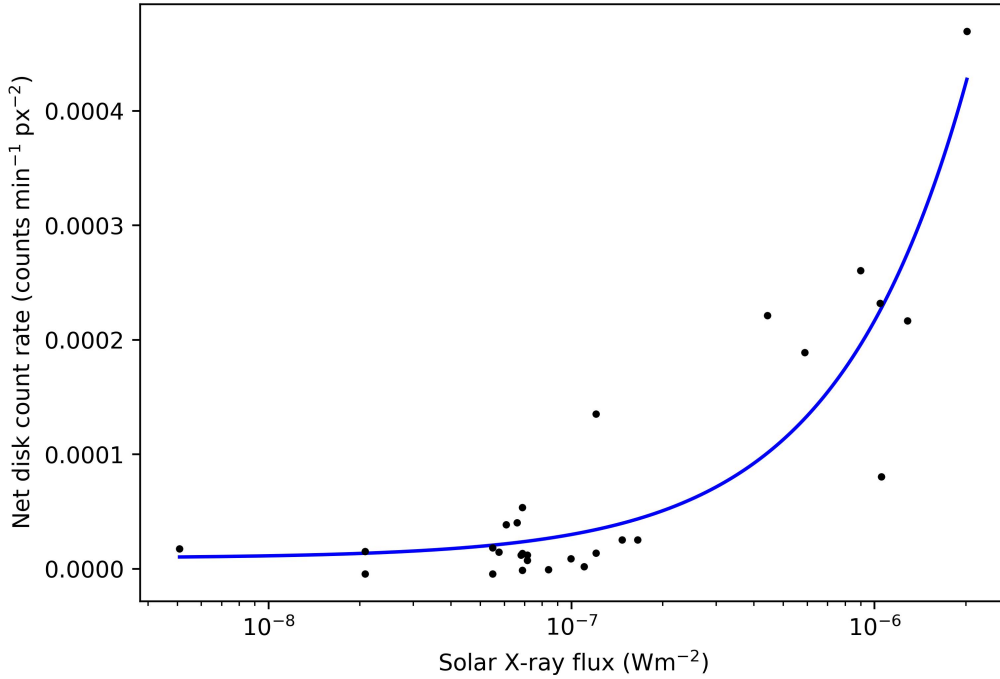


**Figure 6.** Correlation plot between net jovian disk count rates per unit area ( $\text{cts min}^{-1} \text{px}^{-2}$ ) and median GOES solar X-ray flux ( $\text{Wm}^{-2}$ ) over the same observation window. Data are plotted on a log vs linear scale. The linear least squares fit of the data is displayed in blue.

316 pose, we employ Voronoi tessellation (VT) diagrams, based on the VOISE (VORonoi Im-  
 317 age SEgmentation) algorithm (Guio & Achilleos, 2009), which were described in section  
 318 2.2.4. Cases are shown in Figure 7 for observations coinciding with relatively high (a)  
 319 and low (b) solar activity, using the same observations that were displayed in Figure 5.

320 In order to represent Jupiter's internal magnetic field, we have incorporated the  
 321 JRM09 (Juno Reference Model through Perijove 9) internal field model (J. E. Conner-  
 322 ney et al., 2018), a spherical harmonic model of the magnetic field of Jupiter obtained  
 323 from vector magnetic field observations taken by the Juno spacecraft during its first nine  
 324 polar orbits of the planet. The surface magnetic field iso-contours (yellow) were gener-  
 325 ated using the LesiaMag distribution (Ceconi et al., 2022), are overlaid on the tessel-  
 326 lation plots in Figure 7, and aid in the identification of any spatial preference of the jo-  
 327 vian disk emissions. Also included are the latitudinal boundaries of the disk region (red)  
 328 that were defined previously:  $45^\circ$  SIII latitude in the north and  $-55^\circ$  SIII latitude in the  
 329 south. Although auroral photons are included in the Voronoi tessellation diagrams in Fig-  
 330 ure 7, the planetary disk remains the key region of interest.

331 The result of the high-solar flux case (panel a) is that uniformity is observed across  
 332 the disk, with the majority of polygons having an area  $< 50 \text{ deg}^2$ . Cases of higher solar  
 333 activity are expected to reveal less of the underlying morphology of the disk as the  
 334 expectation would be that stronger solar X-ray flux would dominate the production and  
 335 emission of jovian disk X-rays. Additionally, for observations that have an exposure time  
 336 of roughly one full jovian rotation (like these examples), each longitude would receive  
 337 equal spatial coverage by the Sun. The result being that all longitudes will be illumi-

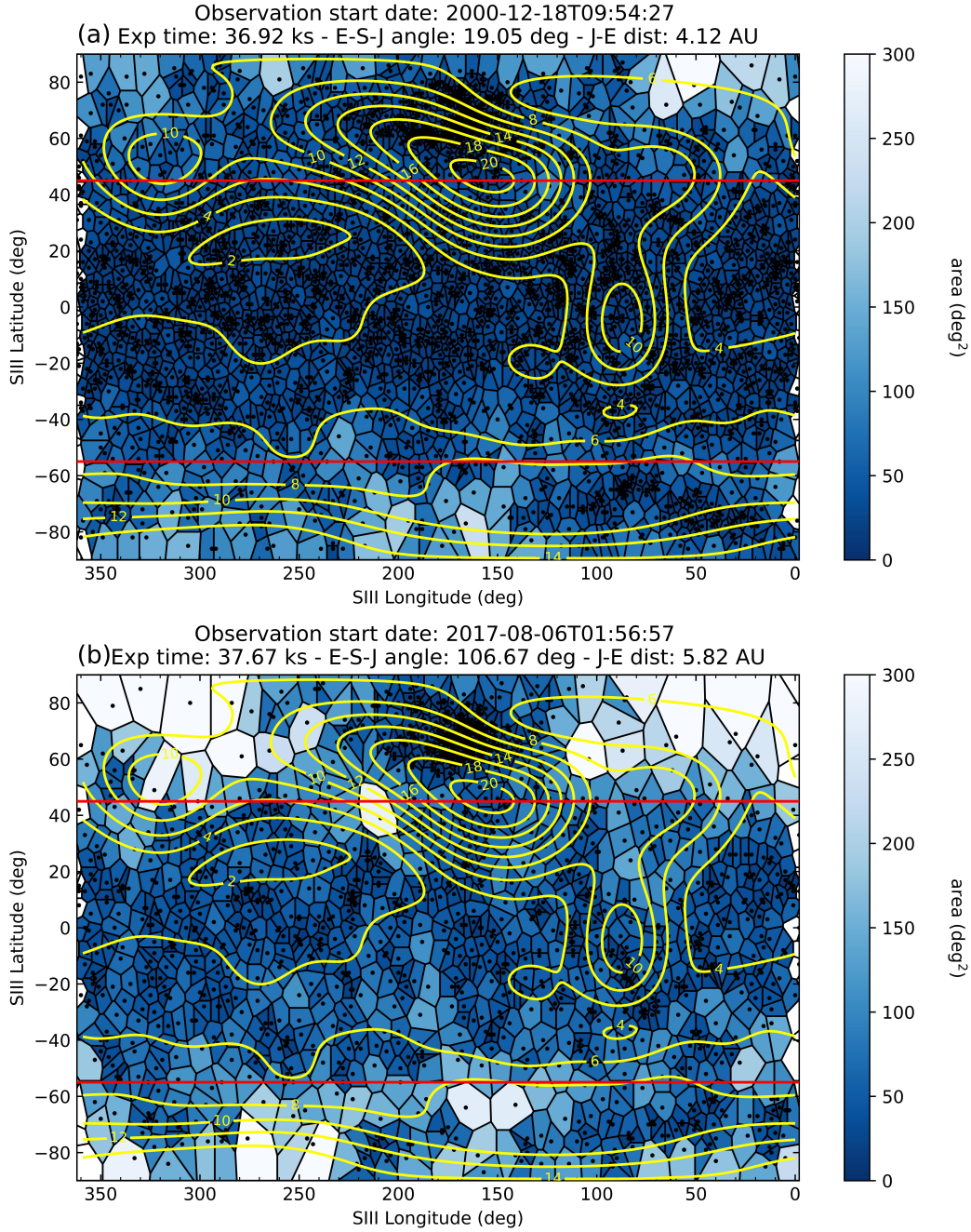


**Figure 7.** Voronoi tessellation diagrams with JRM09 internal magnetic field model overlaid (yellow contours) for observations coinciding with relatively high (a) (ObsID 1862) and low (b) solar activity (ObsID 20002). The borders of each polygon encompass the area around a photon which is closer to that photon than any other. The colourbar represents the area of the polygons ( $\text{deg}^2$ ). Clustering of photons will result in lower area polygons. Red horizontal lines represent the latitude boundaries of the disk region, which are  $45^\circ$  SIII latitude in the north and  $-55^\circ$  SIII latitude in the south.

338  
339

nated by the Sun in equal proportion, making any spatial non-uniformity of the disk X-ray emission unlikely.

340 By contrast, instances of lower solar activity may allow more scope to search for  
 341 distinct local anomalies in disk X-ray morphology (Bhardwaj et al., 2005). Figure 7(b)  
 342 represents a low solar activity case which allows us to search for a potential spatial pref-  
 343 erence to the emission. In this case, the Voronoi tessellation diagram is observed to have  
 344 more variability than its high solar activity counterpart. A greater number of polygons  
 345 are observed with areas  $> 50 \text{ deg}^2$ , while we also see clustering of polygons of smaller  
 346 areas.

347 It is difficult to identify any spatial clustering of jovian disk photons in relation to  
 348 surface magnetic field strength from the tessellation plots in Figure 7 alone, due to the  
 349 fact that the iso-contours differ greatly in terms of area, and also because many of the  
 350 iso-contours traverse the latitude constraints (defined in Figure 4) of the planetary disk  
 351 region. It is evident that there is clearly a great deal of structure in the X-ray cluster-  
 352 ing in both tessellation maps that is well above the statistical fluctuations and does not  
 353 appear to be related to variations in the magnetic field. To extract more information from  
 354 this analysis, we first split our data set into two groups: observations coinciding with (1)  
 355 high and (2) low solar activity. For an observation to be considered to coincide with high  
 356 solar activity, the corresponding peak GOES X-ray light-curve must exceed  $10^{-6} \text{ Wm}^{-2}$ .  
 357 As stated previously, this threshold was chosen because it represents the mean peak flux  
 358 across the data set. A further constraint stated that the observation must encompass  
 359 at least one full jovian rotation. The result was that the high solar activity group con-  
 360 tained 6 HRC-I observations of Jupiter, while the low solar activity group contained 15  
 361 observations. Observations that fall into the high solar activity group are denoted “\*”  
 362 in Table 1, while low solar activity group observations display “†”. This distribution high-  
 363 lights the sparsity of HRC observations of Jupiter during periods of high solar activity,  
 364 which can also be observed in the sunspot plot in Figure 1(a). Of the 7 HRC observa-  
 365 tions that had an exposure time less than one full jovian rotation, none coincided with  
 366 a period of high solar activity.

367 We then investigated the surface magnetic field strength at the location of each of  
 368 the jovian disk photons. The JRM09 model provides magnetic field data with  $1^\circ$  SIII  
 369 longitude  $\times 1^\circ$  SIII latitude resolution. For each observation, a histogram is produced  
 370 whereby the disk counts are binned into 0.5 Gauss bins (10,000 Gauss = 1 Tesla), and  
 371 these counts are then normalised by the area of the disk that is contained within each  
 372 of the magnetic field bins. The histograms are then combined in Figure 8 (grey lines)  
 373 so that a superposed epoch analysis can be performed on both the high (panel a) and  
 374 low (panel b) solar activity groups. The scaled sum (blue), which includes  $3\sigma$  error bars  
 375 (shaded grey area), was calculated by finding the mean counts/sq-degree within each 0.5  
 376 Gauss bin. Also included is a latitudinal dependence function (red) to account for scat-  
 377 tering across the curved surface of the planet. Bhardwaj et al. (2006) found that the low-  
 378 to middle-latitude jovian X-ray photons are consistent with the cosine-squared depen-  
 379 dence expected from a disk of uniform surface brightness. To examine how much of an  
 380 effect the scattering angle has when observing the jovian disk, we therefore apply a  $\cos^2\theta$   
 381 distribution over our disk region latitude range ( $-55^\circ, +45^\circ$ ). This scattering distribution  
 382 is also normalised by the disk area within each magnetic field bin. The sharp increase  
 383 in the normalised latitudinal dependence at high surface magnetic field strengths is due  
 384 to the fact that very few locations within the disk region have such high associated mag-  
 385 netic field strengths. Therefore, even if there are very few photons at these locations, the  
 386 latitudinal dependence will be very high after accounting for the area.

387 In Figure 8, the scaled sum (blue) displays a general increase in mean counts/sq-  
 388 degree over the surface magnetic field strength range 2-3.5 Gauss. This is observed for  
 389 both the high (a) and low (b) solar activity groups, and is followed by a decrease in nor-  
 390 malised counts over the range 4-7.5 Gauss. Over this entire magnetic field range (2-7.5  
 391 Gauss), the latitudinal dependence (red) remains flat, meaning that this increase and  
 392 decrease in the normalised counts is not a latitudinal effect. This feature therefore ap-

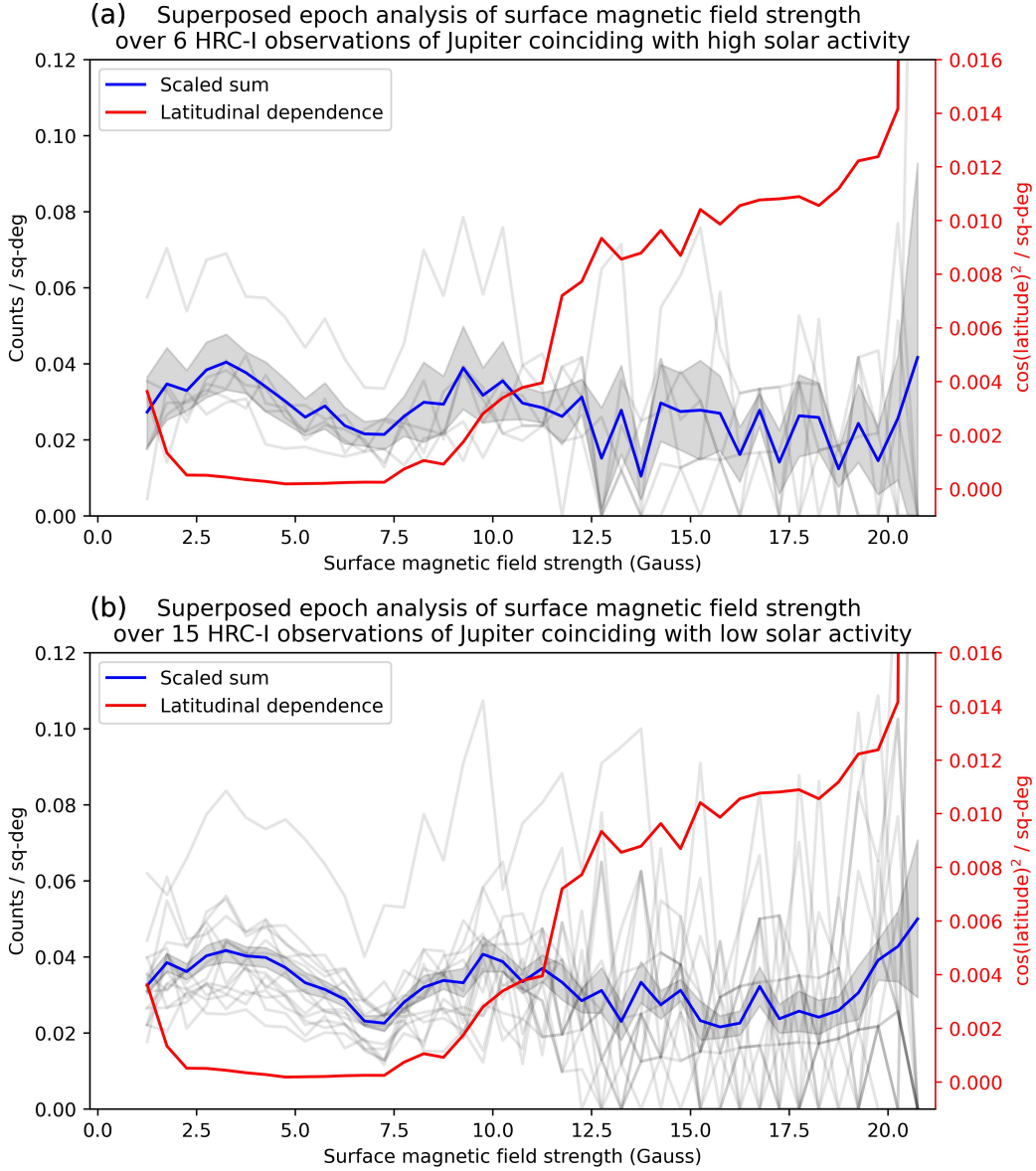


**Figure 8.** Histograms showing jovian disk counts as a function of surface magnetic field strength (Gauss) for (a) 6 HRC observations of Jupiter coinciding with high solar activity and (b) 15 HRC observations coinciding with low solar activity. Data is presented in 0.5 Gauss bins, and counts were normalised by the area of the planetary disk contained within each magnetic field bin (counts/sq-deg). The scaled sum (blue), giving the mean counts/sq-deg, is shown with  $3\sigma$  error bars (shaded grey area). The latitudinal dependence (red) accounts for scattering across the curved surface of the planet using a  $\cos(\text{latitude})^2$  distribution, and is also normalised by area. This is included to examine how much of an effect the scattering angle has when observing the jovian disk.

393 appears to indicate the preference of some jovian disk X-ray emission to come from regions  
 394 of lower magnetic field strength, and there is a sharp drop off when the magnetic field  
 395 strength increases. This indicates the possible presence of another driver of a portion of

396 the jovian disk X-ray emissions, and gives credence to the hypothesis put forward in Waite  
397 et al. (1997) and Gladstone et al. (1998) that a larger atmospheric loss cone in these re-  
398 gions of weaker surface magnetic field strength can lead to the precipitation of otherwise  
399 trapped electrons and ions from the radiation belts into the planet’s upper atmosphere,  
400 where they undergo charge exchange or bremsstrahlung interactions to produce X-rays.  
401 Another interesting result is that this increase and decrease in the normalised counts ap-  
402 pears for both the high (a) and low (b) solar activity groups, suggesting the possibility  
403 that radiation belt precipitation is still observable even in cases of high-solar activity.

404 Numazawa et al. (2019, 2021) investigated emissions from the radiation belts using  
405 X-ray data sets of Jupiter taken by the Suzaku X-ray Imaging Spectrometer (XIS)  
406 (Mitsuda et al., 2007) in 2006 (Ezoe et al., 2010), 2012, and 2014. These observations  
407 revealed diffuse X-ray emission in the 1-5 keV energy range associated with the jovian  
408 inner radiation belts, and this diffuse emission remained observable at solar maximum  
409 in 2014 (Numazawa et al., 2019). Ezoe et al. (2010) suggested that inverse-Compton scat-  
410 tering between ultra-relativistic (tens of MeV) electrons in the radiation belts and vis-  
411 ible solar photons was the most likely cause of this emission.

412 This study sets the foundation for a potential new avenue to use the jovian X-ray  
413 data sets to explore the radiation belts of Jupiter. Kollmann et al. (2021) presented Juno  
414 measurements suggesting that certain magnetic field regions close to the planet are not  
415 expected to be able to trap charged particles. If we consider the spatial analysis presented  
416 in this study (e.g. Figure 7), and use the latest magnetic field (JRM33, J. Connerney  
417 et al. (2022)) and current sheet (J. Connerney et al., 2020) models to map X-ray pho-  
418 tons on Jupiter’s surface to their source locations within the jovian magnetosphere (us-  
419 ing e.g., the JupiterMag package, James et al. (2022), or the LesiaMag distribution, Cecconi  
420 et al. (2022)), we can potentially locate and isolate the regions within the jovian disk where  
421 radiation belt precipitation is most likely to occur. This could potentially benefit col-  
422 laborative observing efforts in the future by enabling remote tracking of the loss of ra-  
423 diation belt particles into the jovian atmosphere.

## 424 4 Summary

425 Here, we present a statistical study of the jovian disk emissions using 19 years of  
426 Chandra HRC-I data. We implement a Pulse Invariant filtering method to minimise back-  
427 ground and ensure consistency across our data set in relation to instrument degradation  
428 over time. We compare the Chandra data to solar X-ray flux data from the GOES X-  
429 ray Sensor (XRS), resulting in a strong correlation between the two data sets, with a Pear-  
430 son’s Correlation Coefficient of 0.9. Incorporating Voronoi tessellation diagrams, we iden-  
431 tify a clustering effect that, on initial inspection, appears to be unrelated to variations  
432 in the surface magnetic field strength. However, after grouping cases of high and low so-  
433 lar activity, and comparing normalised counts to surface magnetic field strength, we find  
434 a preference for the disk emission in the 2-3.5 Gauss region of surface magnetic field strength.  
435 This suggests that the production of the disk X-ray emissions is predominantly governed  
436 by solar activity, but may also contain the imprint of radiation belt precipitation into  
437 the atmosphere.

## 438 Acknowledgments

439 We thank the Chandra team for all their support with this study. We thank the SIDC  
440 team for provision of sunspot numbers: SIDC team, World Data Center for the Sunspot  
441 Index, RoyalObservatory of Belgium, Monthly Report on the International Sunspot Num-  
442 ber C. M. Jackman’s, S. C. McEntee’s and C. K. Louis’s work at DIAS was supported  
443 by Science Foundation Ireland award 18/FRL/6199. D. M. Weigt is supported by the  
444 Science and Technology Facilities Council (STFC) studentship ST/S505705/1.

## Data Availability Statement

*NASA Chandra X-ray Observatory* observations used in this study are available from the Chandra Data Archive <http://cda.harvard.edu/chaser/>. *NOAA's GOES X-ray Sensor* data used in this study can be found at <https://www.ngdc.noaa.gov/stp/satellite/goes/index.html>. The *online catalogue of the sunspot index* is available at <http://www.sidc.be/sunspot-data/>. Data analysis methods and code for this work are provided at <https://doi.org/10.5281/zenodo.5657142>.

## References

- Bhardwaj, A., Branduardi-Raymont, G., Elsner, R. F., Gladstone, G. R., Ramsay, G., Rodriguez, P., ... Cravens, T. E. (2005, 2). Solar control on jupiter's equatorial x-ray emissions: 26-29 november 2003 xmm-newton observation. *Geophysical Research Letters*, *32*, 1-5. doi: 10.1029/2004GL021497
- Bhardwaj, A., Eisner, R. F., Gladstone, G. R., Waite, J. H., Branduardi-Raymont, G., Cravens, T. E., & Ford, P. G. (2006, 11). Low- to middle-latitude x-ray emission from jupiter. *Journal of Geophysical Research: Space Physics*, *111*. doi: 10.1029/2006JA011792
- Bolton, S. J., Lunine, J., Stevenson, D., Connerney, J. E. P., Levin, S., Owen, T. C., ... Thorpe, R. (2017, November). The Juno Mission. *Space Science Reviews*, *213*(1-4), 5-37. doi: 10.1007/s11214-017-0429-6
- Branduardi-Raymont, G., Bhardwaj, A., Elsner, R. F., Gladstone, G. R., Ramsay, G., Rodriguez, P., ... Cravens, T. E. (2007, 6). Latest results on jovian disk x-rays from xmm-newton. *Planetary and Space Science*, *55*, 1126-1134. doi: 10.1016/j.pss.2006.11.017
- Branduardi-Raymont, G., Bhardwaj, A., Elsner, R. F., & Rodriguez, P. (2010). X-rays from saturn: A study with xmm-newton and chandra over the years 2002-05. *Astronomy and Astrophysics*, *510*. doi: 10.1051/0004-6361/200913110
- Branduardi-Raymont, G., Elsner, R. F., Galand, M., Grodent, D., Cravens, T., Ford, P., ... Waite Jr, J. (2008). Spectral morphology of the x-ray emission from jupiter's aurorae. *Journal of Geophysical Research: Space Physics*, *113*(A2).
- Cecconi, B., Louis, C. K., Lamy, L., Zarka, P., & Hess, S. L. G. (2022, October). *LESIA-Mag\_IDL: LESIA Planetary Magnetic Field IDL computing scripts*. Zenodo. Retrieved from <https://doi.org/10.5281/zenodo.7235424> doi: 10.5281/zenodo.7235424
- Connerney, J., Timmins, S., Herceg, M., & Joergensen, J. (2020). A jovian magnetodisc model for the juno era. *Journal of Geophysical Research: Space Physics*, *125*(10), e2020JA028138.
- Connerney, J., Timmins, S., Oliverson, R., Espley, J., Joergensen, J., Kotsiaros, S., ... others (2022). A new model of jupiter's magnetic field at the completion of juno's prime mission. *Journal of Geophysical Research: Planets*, *127*(2), e2021JE007055.
- Connerney, J. E., Kotsiaros, S., Oliverson, R. J., Espley, J. R., Joergensen, J. L., Joergensen, P. S., ... Levin, S. M. (2018, 3). A new model of jupiter's magnetic field from juno's first nine orbits. *Geophysical Research Letters*, *45*, 2590-2596. doi: 10.1002/2018GL077312
- Cravens, T. E., Clark, J., Bhardwaj, A., Elsner, R., Waite, J. H., Maurellis, A. N., ... Branduardi-Raymont, G. (2006, 7). X-ray emission from the outer planets: Albedo for scattering and fluorescence of solar x rays. *Journal of Geophysical Research: Space Physics*, *111*. doi: 10.1029/2005JA011413
- Dunn, W., Ness, J.-U., Lamy, L., Tremblay, G., Branduardi-Raymont, G., Snios, B., ... Wibisono, A. (2021). A low signal detection of x-rays from uranus. *Journal of Geophysical Research: Space Physics*, *126*(4), e2020JA028739.
- Dunn, W. R., Branduardi-Raymont, G., Carter-Cortez, V., Campbell, A., Elsner, R.,

- 497 Ness, J. U., ... Achilleos, N. (2020a, 6). Jupiter's x-ray emission during the  
498 2007 solar minimum. *Journal of Geophysical Research: Space Physics*, 125.  
499 doi: 10.1029/2019JA027219
- 500 Elsner, R. F., Lugaz, N., Waite, J. H., Cravens, T. E., Gladstone, G. R., Ford,  
501 P., ... Majeed, T. (2005, January). Simultaneous Chandra X ray, Hubble  
502 Space Telescope ultraviolet, and Ulysses radio observations of Jupiter's au-  
503 rora. *Journal of Geophysical Research (Space Physics)*, 110(A1), A01207. doi:  
504 10.1029/2004JA010717
- 505 Elsner, R. F., Ramsey, B. D., Waite, J. H., Rehak, P., Johnson, R. E., Cooper, J. F.,  
506 & Swartz, D. A. (2005, 11). X-ray probes of magnetospheric interactions with  
507 jupiter's auroral zones, the galilean satellites, and the io plasma torus. *Icarus*,  
508 178, 417-428. doi: 10.1016/j.icarus.2005.06.006
- 509 Ezoe, Y., Ishikawa, K., Ohashi, T., Miyoshi, Y., Terada, N., Uchiyama, Y., & Ne-  
510 goro, H. (2010, February). Discovery of Diffuse Hard X-Ray Emission Around  
511 Jupiter with Suzaku. *The Astrophysical Journal Letters*, 709(2), L178-L182.  
512 doi: 10.1088/2041-8205/709/2/L178
- 513 Gladstone, G. R., Waite, J. H., Grodent, D., Lewis, W. S., Crary, F. J., Elsner,  
514 R. F., ... Cravens, T. E. (2002, February). A pulsating auroral X-ray hot spot  
515 on Jupiter. *Nature*, 415(6875), 1000-1003. doi: 10.1038/4151000a
- 516 Gladstone, G. R., Waite, J. H., & Lewis, W. S. (1998). Secular and local time de-  
517 pendence of jovian x ray emissions. *Journal of Geophysical Research E: Plan-  
518 ets*, 103, 20083-20088. doi: 10.1029/98je00737
- 519 Guio, P., & Achilleos, N. (2009, September). The VOISE algorithm: a versa-  
520 tile tool for automatic segmentation of astronomical images. *Monthly No-  
521 tices of the Royal Astronomical Society*, 398(3), 1254-1262. doi: 10.1111/  
522 j.1365-2966.2009.15218.x
- 523 Houston, S., Cravens, T., Schultz, D., Gharibnejad, H., Dunn, W., Haggerty, D., ...  
524 Ozak, N. (2020). Jovian auroral ion precipitation: X-ray production from oxy-  
525 gen and sulfur precipitation. *Journal of Geophysical Research: Space Physics*,  
526 125(2), e2019JA027007.
- 527 Jackman, C. M., Knigge, C., Altamirano, D., Gladstone, R., Dunn, W., Elsner, R.,  
528 ... Ford, P. (2018, 11). Assessing quasi-periodicities in jovian x-ray emis-  
529 sions: Techniques and heritage survey. *Journal of Geophysical Research: Space  
530 Physics*, 123, 9204-9221. doi: 10.1029/2018JA025490
- 531 James, M. K., Wilson, R. J., Vogt, M. F., Provan, G., Kamran, A., Brennan, M. J.,  
532 & Cowley, S. W. H. (2022, September). *Jupitermag*. Zenodo. Retrieved from  
533 <https://doi.org/10.5281/zenodo.7074815> (If you use this software, please  
534 cite it using the metadata from this file.) doi: 10.5281/zenodo.7074815
- 535 Jansen, F., Lumb, D., Altieri, B., Clavel, J., Ehle, M., Erd, C., ... Vacanti, G.  
536 (2001, January). XMM-Newton observatory. I. The spacecraft and operations.  
537 *Astronomy and Astrophysics*, 365, L1-L6. doi: 10.1051/0004-6361:20000036
- 538 Kollmann, P., Clark, G., Paranicas, C., Mauk, B., Roussos, E., Nnon, Q., ...  
539 Rymer, A. (2021, 4). Jupiter's ion radiation belts inward of europa's or-  
540 bit. *Journal of Geophysical Research: Space Physics*, 126. doi: 10.1029/  
541 2020JA028925
- 542 Maurellis, A. N., Cravens, T. E., Gladstone, G. R., Waite, J. H., & Acton, L. W.  
543 (2000, 5). Jovian x-ray emission from solar x-ray scattering. *Geophysical  
544 Research Letters*, 27, 1339-1342. doi: 10.1029/1999GL010723
- 545 McEntee, S. (2021, November). *SeanMcEntee/CXO\_and\_GOES\_analyses: Release  
546 of alternative go\_chandra and new PI filtering method for analysing Jupiter's  
547 X-rays using Chandra HRC-I*. Zenodo. Retrieved from [https://doi.org/  
548 10.5281/zenodo.5657142](https://doi.org/10.5281/zenodo.5657142) doi: 10.5281/zenodo.5657142
- 549 Metzger, A. E., Luthey, J. L., Gilman, D. A., Hurley, K. C., Schnopper, H. W.,  
550 Seward, F. D., & Sullivan, J. D. (1983, October). The detection of x rays  
551 from Jupiter. *Journal of Geophysical Research*, 88(A10), 7731-7741. doi:

- 552 10.1029/JA088iA10p07731  
553 Mitsuda, K., Bautz, M., Inoue, H., Kelley, R. L., Koyama, K., Kunieda, H., ...  
554 Yoshida, A. (2007, January). The X-Ray Observatory Suzaku. *Publications of*  
555 *the Astronomical Society of Japan*, 59, S1-S7. doi: 10.1093/pasj/59.sp1.S1  
556 Moore, K. M., Yadav, R. K., Kulowski, L., Cao, H., Bloxham, J., Connerney,  
557 J. E. P., ... Levin, S. M. (2018, September). A complex dynamo inferred from  
558 the hemispheric dichotomy of Jupiter's magnetic field. *Nature*, 561(7721),  
559 76-78. doi: 10.1038/s41586-018-0468-5  
560 Numazawa, M., Ezoe, Y., Ishikawa, K., Ohashi, T., Miyoshi, Y., Kimura, T., ...  
561 Branduardi-Raymont, G. (2019, October). Suzaku observation of Jupiter's  
562 X-rays around solar maximum. *Publications of the Astronomical Society of*  
563 *Japan*, 71(5), 93. doi: 10.1093/pasj/psz077  
564 Numazawa, M., Ezoe, Y., Ohashi, T., Ishikawa, K., Miyoshi, Y., Shiota, D., ...  
565 Branduardi-Raymont, G. (2021, August). Suzaku observations of Jovian dif-  
566 fuse hard X-ray emission. *Publications of the Astronomical Society of Japan*,  
567 73(4), 894-911. doi: 10.1093/pasj/psab053  
568 Posson-Brown, J., & Kashyap, V. (2007). HRC-I gain correction. In O. H. Siegmund  
569 (Ed.), *Uv, x-ray, and gamma-ray space instrumentation for astronomy xv* (Vol.  
570 6686, pp. 245 – 254). SPIE. Retrieved from [https://doi.org/10.1117/](https://doi.org/10.1117/12.740147)  
571 [12.740147](https://doi.org/10.1117/12.740147) doi: 10.1117/12.740147  
572 Stallard, T. S., Burrell, A. G., Melin, H., Fletcher, L. N., Miller, S., Moore, L., ...  
573 Johnson, R. E. (2018). Identification of jupiters magnetic equator through h3+  
574 ionospheric emission. *Nature Astronomy*, 2(10), 773–777.  
575 Tobiska, W. K., & Eparvier, F. G. (1998, January). EUV97: Improvements to  
576 EUV Irradiance Modeling in the Soft X-Rays and FUV. *Solar Physics*, 177,  
577 147-159. doi: 10.1023/A:1004931416167  
578 Waite, J. H., Gladstone, G. R., Lewis, W. S., Drossart, P., Cravens, T. E., Maurellis,  
579 A. N., ... Miller, S. (1997, April). Equatorial X-ray emissions: Implica-  
580 tions for Jupiter's high exospheric temperatures. *Science*, 276, 104-108. doi:  
581 10.1126/science.276.5309.104  
582 Weigt, D., Dunn, W. R., Jackman, C., Kraft, R., Branduardi-Raymont, G., Nichols,  
583 J., ... Gladstone, G. (2021). Searching for saturns x-rays during a rare jupiter  
584 magnetotail crossing using chandra. *Monthly Notices of the Royal Astronomi-  
585 cal Society*, 506(1), 298–305.  
586 Weigt, D. M., Jackman, C. M., Dunn, W. R., Gladstone, G. R., Vogt, M. F.,  
587 Wibisono, A. D., ... Kraft, R. P. (2020, 4). Chandra observations of jupiter's  
588 x-ray auroral emission during juno apojove 2017. *Journal of Geophysical*  
589 *Research: Planets*, 125. doi: 10.1029/2019JE006262  
590 Weigt, D. M., Jackman, C. M., Vogt, M. F., Manners, H., Dunn, W. R., Gladstone,  
591 G. R., ... McEntee, S. C. (2021, 9). Characteristics of jupiter's x-ray auroral  
592 hot spot emissions using chandra. *Journal of Geophysical Research: Space*  
593 *Physics*, 126. doi: 10.1029/2021JA029243  
594 Weisskopf, M. C., Tananbaum, H. D., Van Speybroeck, L. P., & O'Dell, S. L. (2000,  
595 July). Chandra X-ray Observatory (CXO): overview. In J. E. Truemper &  
596 B. Aschenbach (Eds.), *X-ray optics, instruments, and missions iii* (Vol. 4012,  
597 p. 2-16). doi: 10.1117/12.391545